IEEE Photonics Journal
An IEEE Photonics Society Publication

Open Access

Photonic Nanojet Analysis by Spectral Element Method

Volume 6, Number 5, October 2014

I. Mahariq
M. Kuzuoğlu
I. H. Tarman
H. Kurt

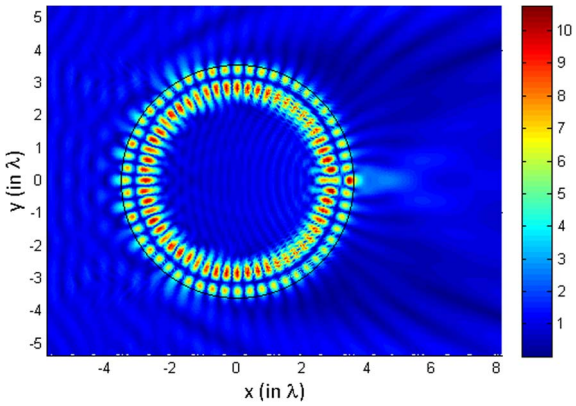

DOI: 10.1109/JPHOT.2014.2361615
1943-0655

IEEE photonics SOCIETY

IEEE

Photonic Nanojet Analysis by Spectral Element Method

I. Mahariq,[1,2] M. Kuzuoğlu,[3] I. H. Tarman,[2] and H. Kurt[1]

[1]Department of Electrical and Electronics Engineering, Faculty of Engineering, TOBB University of Economics and Technology, 06560 Ankara, Turkey
[2]Department of Engineering Sciences, Faculty of Engineering, Middle East Technical University, 06531 Ankara, Turkey
[3]Department of Electrical and Electronics Engineering, Faculty of Engineering, Middle East Technical University, 06800 Ankara, Turkey

DOI: 10.1109/JPHOT.2014.2361615

Manuscript received August 30, 2014; revised September 25, 2014; accepted September 25, 2014. Date of publication October 7, 2014; date of current version October 15, 2014. The work of I. Mahariq was supported by the Technical Research Council of Turkey (TUBITAK). The work of H. Kurt was supported in part by the Turkish Academy of Sciences. Corresponding author: I. Mahariq (e-mail: ibmahariq@gmail.com).

Abstract: Although it is known that the spectral element method (SEM) has both high accuracy and a lower computational cost when compared with finite-element or finite-difference methods, the SEM is not widely utilized in the modeling of boundary value problems in electromagnetics. This paper provides a 2-D formulation of the well-known perfectly-matched-layer approach in the context of the SEM for the frequency-domain electromagnetic problems in which dielectric scatterers are involved. The formulation is then utilized to numerically study photonic nanojets after the demonstration of SEM accuracy in an electromagnetic scattering problem. Interesting cases where unusual results are obtained from scattering dielectric cylinders are reported and discussed in this paper. On the other hand, a finite-difference time-domain method that is widely deployed for investigating photonic nanojets is found to fail in successfully capturing such resonance cases. Sharp resonances are characteristic of high-Q cavities and numerical methods with high accuracy, e.g., the SEM can provide superior performance while exploring such resonators.

Index Terms: Spectral element method, finite-difference time-domain method, photonic nanojets, sub-wavelength imaging, whispering gallery modes.

1. Introduction

Computational electromagnetics is heavily used in the study of electromagnetic field interaction with physical objects. Depending on the nature of the problem under study, different numerical techniques are preferably implemented. Spectral element method (SEM) can be considered as a generalization of the finite element method (FEM) with special choice of quadrature integration points and nodal points. What makes SEM worthy to use as a numerical modeling method in computational electromagnetics is its high degree of accuracy and its lower computational cost in terms of CPU time and memory when compared with FEM or finite-difference time-domain (FDTD) method [1]–[3]. These attractive features of SEM are gained from introducing higher degree basis functions that lead to have a minimal number of unknowns. As a result, it is important

to outline the advantageous features of SEM compared to a widely used numerical technique such as FDTD.

Light as an electromagnetic field interacts with different metallic or dielectric objects of any size and shape and provides novel features via scattering, reflection, refraction, and diffraction mechanisms [4], [5]. To be more specific about light interaction with an object, we can assume lossless (absorption free) dielectric micro-cylinders and excitation with a normally incident plane wave. The result of the interaction produces scattered light and strongly focused beam intensity at the back side of the medium (shadow side). Due to unique nature of the light distribution at the focal area, the phenomenon is named as photonic nanojets [6]–[10].

Optical engineering of micron sized dielectric cylinders and spheres produces nano-scale light manipulation. Divergence behavior of the beam whether low or large, location of the focus (inside, at the boundary or outside of the cylinder), field enhancement, and transverse dimension of the spot size compared to the illuminating wavelength (how small with respect to the wavelength) are important parameters for the photonic nanojet. A substantial literature has been devoted to the verification of light focusing of photonic nanojet into sub-diffraction-limited sizes. Squeezing light at the shadow side as well as altering the location of focal point by means of different material and structural parameters (refractive index, radius, deformation, wavelength etc.) are unique properties to create interaction between enhanced intensity and matter. Some of the attractive applications of photonic nanojet include bio-sensing, sub-diffraction-limited size optical imaging, single molecule detection and enhanced Raman scattering [6], [11], [12]. Low-loss optical wave guiding, high density data storage, lithography, high resolution microscopy, and nonlinear optical effects are the other applications of photonic nanojets [13]–[15]. Experimental observation of photonic nanojets generated by latex microspheres of varying diameters was reported in [9]. Low loss optical guiding of light can be accomplished by touching microspheres [14]. Propagation losses as low as 0.08 dB per microsphere was measured in the same study.

Photonic nanojets have been mainly explored by numerical methods based on FDTD analysis [16], [17]. Very fine meshes are required in order to get accurate and reliable results with FDTD method. Besides, the excitation mechanism such as plane wave in free space may restrict the observation of special resonance modes. Later, analytical and semi-analytical attempts were introduced in the literature [7], [18]. The majority of analytical studies are based on Mie theory. Rigorous Mie theory was used to analyze the fundamental properties of the photonic nanojet in [7]. Recasting eigenfunction solution of the Helmholtz equation into a Debye series, [18] provided detailed optics of photonic nanojets on dielectric cylinders.

As mentioned previously, to have accurate results with FDTD method it is necessary for finely discretized mesh which is a huge burden in terms of computational resources. Therefore, it is important to check and verify results with an alternative numerical method. In the present work, SEM is implemented and the spectral properties of the photonic nanojets are captured while light interacts with the wavelength scale dielectric cylinders. A plane wave polarized light with the incident electric field parallel to the cylinder's out of plane axis is used as a source to illuminate each cylinder. We show that SEM is a versatile tool for analyzing light interaction with micro-cylinders especially for capturing resonance modes of whispering gallery type. Meanwhile, FDTD provides spatial field distributions, but it is challenging to capture resonance modes by just exciting the cylinder with a plane wave.

Previously reported results are exactly reproduced in the current study. This validates the accuracy of the formulation and implementation of the numerical analysis based on SEM. More important than that is the observation of the unique light distribution property that is associated with a resonance mode behavior. Depending on the parameters of the micro-cylinder, radius (R) and refractive index (n), strong field enhancement occurs and different number of rings appears within the cylinder. These features can be attributed to whispering gallery modes supporting in micro-cylinders.

The paper is arranged as follows: In Section 2, the formulation of perfectly matched layer (PML) approach in 2-D frequency domain problems involving dielectric scatterers is presented.

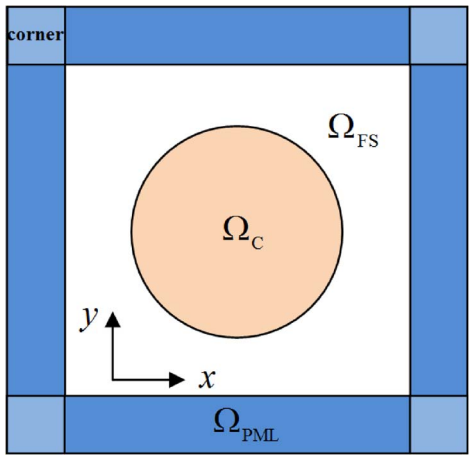

Fig. 1. Definition of the computational domain composed of a dielectric cylinder (Ω_C), embedded in the free space (Ω_{FS}), and truncated by PML boundary.

In Section 3, the approximation of Helmholtz equation by SEM with PML boundary condition is given. Section 4 demonstrates the accuracy of SEM by a numerical example, and Section 5 presents and discusses results of photonic nanojets. Finally, some conclusions are presented in Section 6.

2. Formulation of Scattering Dielectric Cylinders

In general, computational domains in electromagnetic scattering problems are unbounded. Therefore, one needs to truncate the physical domain by the PML being the best approach for domain truncation [19]. In the case of photonic nanojet where the scatterer is assumed to be an infinitely-long dielectric cylinder, the problem can be dealt as a two-dimensional one when an incident plane wave propagating in a direction perpendicular to the cylinder axis. Fig. 1 shows, in the xy-plane, a dielectric cylinder represented by Ω_C, free space region represented by Ω_{FS}, and the PML region denoted by Ω_{PML}, which represents the region surrounding Ω_{FS}. On the outer boundary of Ω_{PML}, zero Dirichlet boundary condition is simply imposed. In Ω_{FS}, the homogenous Helmholtz equation is satisfied:

$$\nabla^2 E_z^s + k^2 E_z^s = 0 \tag{1}$$

in which E_z^s stands for the scattered electric field and polarized in the z-direction (TM_z polarization is considered), and k is the wave number. In Ω_C, the following Helmholtz equation can be derived:

$$\nabla.\left(\frac{1}{\mu_r}\nabla E_z^s\right) + k^2 \varepsilon_r E_z^s = k^2(1-\varepsilon_r)E_z^{inc} \tag{2}$$

where ε_r and μ_r are the relative permittivity and the relative permeability, respectively, and E_z^{inc} stands for the incident plane wave. Throughout this work, we assume that the medium in nonmagnetic ($\mu_r = 1$), and an incident plane wave of the form (with suppressed time dependence $\exp(j\omega t)$):

$$E_z^{inc} = \hat{a}_z \exp(-jkx). \tag{3}$$

In Ω_{PML}, the following set of partial differential equations must be satisfied [20]; in regions having a vertical interface with Ω_{FS}, attenuation of the field is carried out in the x-direction only:

$$\frac{1}{\mathrm{a}^2}\frac{\partial^2 E_z^s}{\partial x^2}+\frac{\partial^2 E_z^s}{\partial y^2}+k^2 E_z^s=0 \tag{4}$$

where a is defined as

$$\mathrm{a}=1+\frac{\alpha}{jk} \tag{5}$$

with α being a real positive constant. In regions having a vertical interface with Ω_{FS}, the attenuation of the field is carried out in the y-direction only. Here, we choose the horizontal and vertical PML regions to be equal in width, hence; the attenuation in the y-direction is governed by

$$\frac{\partial^2 E_z^s}{\partial x^2}+\frac{1}{\mathrm{a}^2}\frac{\partial^2 E_z^s}{\partial y^2}+k^2 E_z^s=0. \tag{6}$$

For a corner region in Ω_{PML}, the attenuation is applied in both directions:

$$\frac{1}{\mathrm{a}^2}\frac{\partial^2 E_z^s}{\partial x^2}+\frac{1}{\mathrm{a}^2}\frac{\partial^2 E_z^s}{\partial y^2}+k^2 E_z^s=0. \tag{7}$$

It is worth pointing out that at the PML-free space interfaces, continuity condition is satisfied [20]. However, one more condition is required which relates the first derivatives of the field in both regions together, i.e., if $x=x_0$ stands for the right-side interface, then we must have

$$\left.\frac{\partial E_z^s}{\partial x}\right|_{-x_0}=\frac{1}{\mathrm{a}}\left.\frac{\partial E_z^s}{\partial x}\right|_{+x_0}. \tag{8}$$

This condition is satisfied when applying integration by parts if (4) and (6) are rewritten as

$$\frac{1}{\mathrm{a}}\frac{\partial^2 E_z^s}{\partial x^2}+\mathrm{a}\frac{\partial^2 E_z^s}{\partial y^2}+\mathrm{a}k^2 E_z^s=0 \tag{9}$$

$$\mathrm{a}\frac{\partial^2 E_z^s}{\partial x^2}+\frac{1}{\mathrm{a}}\frac{\partial^2 E_z^s}{\partial y^2}+\mathrm{a}k^2 E_z^s=0 \tag{10}$$

respectively. After we formulate the governing equations for both boundary (PML) and the interior region (computational domain), we move in the next section for implementing SEM.

3. SEM Formulation

Before proceeding with the formulation of SEM, it would be meaningful to provide a brief overview of SEM and FEM along with their different forms. FEM basically discretizes the computational domain into fine meshes to solve partial differential equations in its equivalent variational form. The aim is to approximate the unknown solution by piecewise linear interpolation functions. Higher-order FEM locally expands the solution into a set of P + 1 linearly independent polynomials [23], [24]. *h*-version FEM fixes the degree of P of the piecewise polynomial basis

functions, but the mesh refinement is carried out to enhance the accuracy of the solution. On the other hand, if there is a modification in the polynomial degree P while keeping the partitioning of domain is kept fixed, then the method is called *p*-version FEM. Lastly, when mesh refinement is combined with degree modification then the method is named *hp*-version FEM.

On the other hand, the spectral method approximates the solution by a truncated series of global basis functions. The expansion of the solution into high-order orthogonal expansions may include Fourier, Chebyshev, or Legendre series. The spectral element method (SEM) contains the high accuracy of the spectral method and geometric flexibility of the finite element method. Hence, SEM is conceptually similar to high-order finite element method. The difference lies in the usage of a specific nodal expansion basis. The Lagrange polynomials through the zeros of the Gauss-Legendre-Lobatto polynomials are the class of nodal high-order spectral elements.

In SEM computational error decreases exponentially as the order of approximating polynomial, therefore a fast convergence of solution to the exact solution is realized with fewer degrees of freedom of the structure in comparison with FEM. Over the course, their interactions resulted in various overlapping variants of these methods [23], [25]. Naturally, our main concern in the manuscript is to be concise and relevant in the presentation of Spectral Element Method, but not thorough. Based on the previous formulation given in Section 2, the problem can be defined as

$$\nabla.\Lambda\nabla E_z^s + \mathrm{a}\varepsilon_r k^2 E_z^s = k^2(1-\varepsilon_r)E_z^{inc} \tag{11a}$$

for $\mathbf{x} = (\mathrm{x}, \mathrm{y}) \in \Omega \subset \Re^2$ subject to the boundary conditions

$$E_z^s|_{\partial\Omega_\mathrm{D}} = \mathrm{f}, \qquad \frac{\partial}{\partial n}E_z^s\bigg|_{\partial\Omega_\mathrm{N}} = \mathrm{g} \tag{11b}$$

on the boundary $\partial\Omega = \partial\Omega_\mathrm{D} \cup \partial\Omega_\mathrm{N}$. Λ is a tensor defined as

$$\Lambda = \begin{bmatrix} \Lambda_{11} & 0 \\ 0 & \Lambda_{22} \end{bmatrix} \tag{11c}$$

where $[\Lambda_{11}\ \Lambda_{22}] = [(1/\mathrm{a})\ \mathrm{a}]$ for the x-decay, $[\Lambda_{11}\ \Lambda_{22}] = [\mathrm{a}\ (1/\mathrm{a})]$ for the y-decay, $[\Lambda_{11}\ \Lambda_{22}] = [(1/\mathrm{a})\ (1/\mathrm{a})]$ for a corner region, and $\mathrm{a} = 1$ for Ω_{FS}, with ε_r being greater than 1 in Ω_C only, and 1 elsewhere.

SEM formulation involves two function spaces, namely, test and trial spaces. An approximate solution to (11a) is sought in the trial space

$$U = \left\{ \mathrm{u} \in \mathrm{H} \quad | \quad \mathrm{u}|_{\partial\Omega_D} = \mathrm{f}, \qquad \frac{\partial}{\partial \mathrm{n}}\mathrm{u}\bigg|_{\partial\Omega_\mathrm{N}} = \mathrm{g} \right\} \tag{12}$$

where u denotes E_z^s. The residual resulting from the substitution of the approximate solution from the trial space into (11a) is then projected onto the test space

$$\mathrm{V} = \left\{ \mathrm{v} \in \mathrm{H} | \mathrm{v}|_{\partial\Omega_D} = 0 \right\} \tag{13}$$

and set to zero:

$$\left(\mathrm{v}, \nabla.\Lambda\nabla\mathrm{u} + \mathrm{a}\varepsilon_r k^2 \mathrm{u} - k^2(1-\varepsilon_r)E_z^{inc}\right)_\omega = 0. \tag{14}$$

This amounts to setting the trial function as exact in the test space. Here, the projection is performed by using the weighted inner product operation

$$(\mathrm{v},\mathrm{u})_{\omega} \equiv \int_{\Omega} \omega\, \bar{\mathrm{v}}\, \mathrm{u}\, \mathrm{d}\mathbf{x} \tag{15}$$

in the Hilbert space H and overbar denotes complex conjugation. The projection procedure leads to the variational (weak) form

$$\int_{\Omega} \nabla(\omega\bar{\mathrm{v}})\cdot\Lambda\nabla\,\mathrm{u}\,\mathrm{dx} - \mathrm{a}k^2\int_{\Omega}\omega\bar{\mathrm{v}}\,\mathrm{u}\,\mathrm{dx} = \int_{\partial\Omega_N}\omega\bar{\mathrm{v}}\,\mathrm{g}\,\mathrm{dx} - k^2(1-\varepsilon_r)\int_{\Omega}\omega\bar{\mathrm{v}}\,E_z^{inc}\,\mathrm{dx} \tag{16}$$

after integration by parts that introduces the boundary integrals over the Neumann boundary $\partial\Omega_{\mathrm{N}}$. The nonhomogeneous Dirichlet boundary conditions are then introduced by decomposing the trial function as follows:

$$\mathrm{u} = \mathrm{u_h} + \mathrm{u_b},\ \text{where } \mathrm{u_h}|_{\partial\Omega_{\mathrm{D}}} = 0, \quad \text{and } \mathrm{u_b}|_{\partial\Omega_{\mathrm{D}}} = \mathrm{f} \tag{17}$$

and by substituting into (16) resulting in

$$\int_{\Omega}\nabla(\omega\,\bar{\mathrm{v}})\cdot\ \Lambda\nabla\mathrm{u_h}\,\mathrm{d}\mathbf{x} - \mathrm{a}k^2\int_{\Omega}\omega\bar{\mathrm{v}}\,\mathrm{u_h}\,\mathrm{dx} = -\int_{\Omega}\nabla(\omega\bar{\mathrm{v}})\cdot\Lambda\nabla\,\mathrm{u_b}\,\mathrm{dx}$$
$$+\mathrm{a}k^2\int_{\Omega}\omega\bar{\mathrm{v}}\,\mathrm{u_b}\,\mathrm{dx}\int_{\partial\Omega_{\mathrm{N}}}\omega\bar{\mathrm{v}}\,g\,\mathrm{dx} - k^2(1-\varepsilon_r)\int_{\Omega}\omega\bar{\mathrm{v}}\,E_z^{inc}\mathrm{dx}. \tag{18}$$

The boundary conditions are now in place in the variational form with the particular solution $\mathrm{u_b}$ satisfying the nonhomogeneous Dirichlet boundary condition. The next step in the SEM formulation is the adaptation to arbitrary domain geometry. For this purpose, the domain Ω is partitioned into mutually disjoint elements Ω^{e}

$$\Omega = \bigcup_{\mathrm{e}=1}^{\mathrm{M}}\Omega^{\mathrm{e}} \tag{19}$$

and introduced into the variational form to yield

$$\int_{\Omega}\omega\bar{\mathrm{v}}\,\mathrm{u_h}\ \mathrm{d}\mathbf{x} = \sum_{\mathrm{e}=1}^{M}\int_{\Omega^{\mathrm{e}}}\omega\bar{\mathrm{v}}\,\mathrm{u_h}\,\mathrm{d}\mathbf{x} \tag{20}$$

by the linearity of integration operation. In order to standardize the integral operations, the standard square element is introduced as

$$\Omega^{\mathrm{std}} = \left\{(\xi,\eta)\in\Re^2 \quad | \quad -1\le\xi\le 1, -1\le\eta\le 1\right\} \tag{21}$$

and connected to each quadrilateral element Ω^{e} through the mapping

$$x = \chi_1^{\mathrm{e}}(\xi,\eta), \qquad y = \chi_2^{\mathrm{e}}(\xi,\eta). \tag{22}$$

This also facilitates the integral operations over a general quadrilateral element Ω^{e} with curved sides. The operations can then be converted using the rules

$$\begin{bmatrix} dx \\ dy \end{bmatrix} = \underbrace{\begin{bmatrix} \frac{\partial \chi_1^e}{\partial \xi} & \frac{\partial \chi_1^e}{\partial \eta} \\ \frac{\partial \chi_2^e}{\partial \xi} & \frac{\partial \chi_2^e}{\partial \eta} \end{bmatrix}}_{J} \begin{bmatrix} d\xi \\ d\eta \end{bmatrix}, \quad \nabla = \begin{bmatrix} \frac{\partial}{\partial x} \\ \frac{\partial}{\partial y} \end{bmatrix} = \frac{1}{|J|} \begin{bmatrix} \frac{\partial \chi_2^e}{\partial \eta} & -\frac{\partial \chi_1^e}{\partial \eta} \\ -\frac{\partial \chi_2^e}{\partial \xi} & \frac{\partial \chi_1^e}{\partial \xi} \end{bmatrix} \begin{bmatrix} \frac{\partial}{\partial \xi} \\ \frac{\partial}{\partial \eta} \end{bmatrix} \tag{23}$$

where $|\mathbf{J}|$ is the determinant of the Jacobian $\mathbf{J}$.

For the numerical implementation, the trial and test spaces must be taken as finite dimensional spaces and a spatial discretization needs to be introduced in order to facilitate the numerical evaluation of the derivatives and the integrals. These requirements are met by choosing the space of polynomials, spanned, in particular, by Jacobi polynomials as eigenfunctions of singular Sturm-Liouville differential operator [3]. This choice, in turn, provides numerically stable interpolation and highly accurate quadrature integration approximation techniques by using the nodes and the weights associated with the Jacobi polynomials. In particular, Legendre polynomials are the convenient choice in that they are orthogonal under the weighted inner product with unity weight $\omega = 1$. The associated roots ς_m as nodes provide the stable form of interpolation

$$u(\varsigma) = \sum_{m=0}^{N} u(\varsigma_m) L_m(\varsigma) \tag{24}$$

where L denotes respective Lagrange interpolants with the typical form

$$L_k(\varsigma) = \prod_{\substack{\ell=0 \\ \ell \neq k}}^{N} \frac{(\varsigma - \varsigma_\ell)}{(\varsigma_k - \varsigma_\ell)} \tag{25}$$

satisfying the cardinality property $L_k(\varsigma_\ell) = \delta_{k\ell}$. The derivatives may also be evaluated by

$$\frac{d}{d\varsigma} u(\varsigma)\Big|_{\varsigma_k} = \sum_{m=0}^{N} u(\varsigma_m) L'_m(\varsigma_k) = \sum_{m=0}^{N} u(\varsigma_m) \underbrace{L'_m(\varsigma_k)}_{D_{km}} \tag{26}$$

where D_{km} is referred to as the differentiation matrix. It further provides Gauss–Legendre–Lobatto (GLL) quadrature

$$\int_{-1}^{1} u(\varsigma)\, d\varsigma = \sum_{k=0}^{N} \varpi_k u(\varsigma_k) \tag{27}$$

which is exact for the integrand of a polynomial of degree $\leq 2N - 1$. These can easily be extended to two dimensions over the tensor grid (ξ_k, η_ℓ) with the mapping functions $\chi_i(\xi, \eta)$ constructed using the linear blending function approach [21], [22].

4. Accuracy of SEM

Although the accuracy of SEM has been investigated in many researches, we demonstrate in this work a problem where the analytical solution is available and hence; a comparison with SEM solutions can be carried out. The reason for this demonstration is to emphasize on the

TABLE 1

The maximum relative error obtained by SEM for the perfectly conducting scattering cylinder of radius $R = 0.5\lambda$ as number of nodes (N) increases

N	7	8	9	10	11	12	13	14	15
Err	3.1E-03	4.4E-04	8.0E-05	1.6E-05	4.5E-06	9.2E-07	3.8E-07	8.3E-8	4.7E-8

accuracy SEM in the frequency-domain while studying electromagnetic scattering problems. For this purpose, we considered an infinitely-long perfectly conducting cylinder (PEC), and an incident plane wave propagating in the x-direction. The cylinder is centered at the origin in the xy-plane and has a radius of R. The analytical solution of the scattered field can be expressed in cylindrical coordinates in terms of Bessel and Hankel functions as follows:

$$E_z^s = -E_0 \sum_{n=-\infty}^{\infty} (-\mathrm{j})^n \frac{\mathrm{J_n}(kR)\mathrm{H_n^{(2)}}(k\rho)\mathrm{e}^{\mathrm{j}n\phi}}{\mathrm{H_n^{(2)}}(kR)} \tag{28}$$

where $\mathrm{J_n}$ and $H_n^{(2)}$ denote Bessel function of the first kind and Hankel function of the second kind of *nth* order, respectively, ρ is the Euclidean distance from the z-axis to a point lying outside the cylinder, and ϕ is the azimuth angle. Zero Dirichlet boundary condition is imposed on $\partial\Omega_{PML}$, and the solution given in (28) is imposed on the boundary $\partial\Omega_C$. Table 1 shows the maximum relative error for the PEC case as the number of points per wavelength (N) is increased for $R = 0.5\lambda$, with λ being the wavelength, and $2\lambda \times 2\lambda$ being the dimensions of the surrounding free space region, Ω_{FS}. The error measure is defined as

$$\mathrm{Err} = \max_i \frac{\left|E^s_{z,\mathrm{analytical}} - E^s_{z,\mathrm{SEM}}\right|}{\left|E^s_{z,\mathrm{analytical}}\right|} \tag{29}$$

where $E^s_{z,\mathrm{analytical}}$ and $E^s_{z,\mathrm{SEM}}$ are the analytical solution and the SEM solution, respectively, at the *ith* node corresponding to Ω_{FS}. It is obvious that although this problem is composed of deformed elements (because of having curved boundaries representing the PEC cylinder), if the number of points per wavelength is chosen around 14 or 15 points, very accurate results can be guaranteed. We have tested our SEM codes in several examples; however, we chose to include this demonstration because of the existence of a circular subdomain.

After presenting the accuracy of the SEM we apply the same formulation for the study of light interaction with dielectric micro-cylinders in the next section.

5. SEM Results of Dielectric Cylinders

Lagrangian basis polynomials associated with a tensor product grid of Gauss-Lobatto-Legendre (GLL) nodes are used to build a nodal basis for a reference element of dimensions $[-1, 1] \times [-1, 1]$. Fig. 2 illustrates an example of such a grid for a ninth-order polynomial space (nodes are represented by intersections between the horizontal and vertical lines). The elements in the physical domain are mapped to this reference element.

A possible discretization of the computational domain when the dielectric cylinder radius is $R = 3.5\lambda$, is shown in Fig. 3 for $N \times N = 9 \times 9$ in each element for demonstration purpose. However, in this work, finer resolutions are considered depending on R, for instance when $R = 3.5\lambda$, the grid 30×30 in each element is considered when the domain elements are chosen as shown in Fig. 3 in order to achieve approximately 14 points per wavelength. It is important to mention that the number of elements should be increased as the radius increases due to the distribution nature of GLL nodes.

Typical plots of photonic nanojets are illustrated in Fig. 4 as obtained by SEM for the following cylinder radius R, and the corresponding refractive index n of the cylinder when embedded within

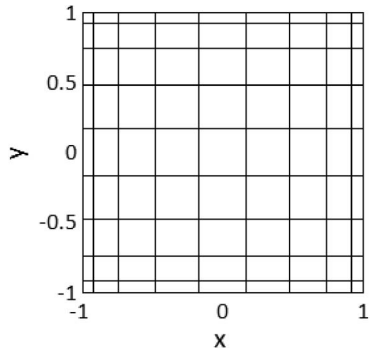

Fig. 2. GLL grid nodes on the reference element for $N \times N = 10 \times 10$ (nodes are represented by intersections between the vertical and horizontal lines).

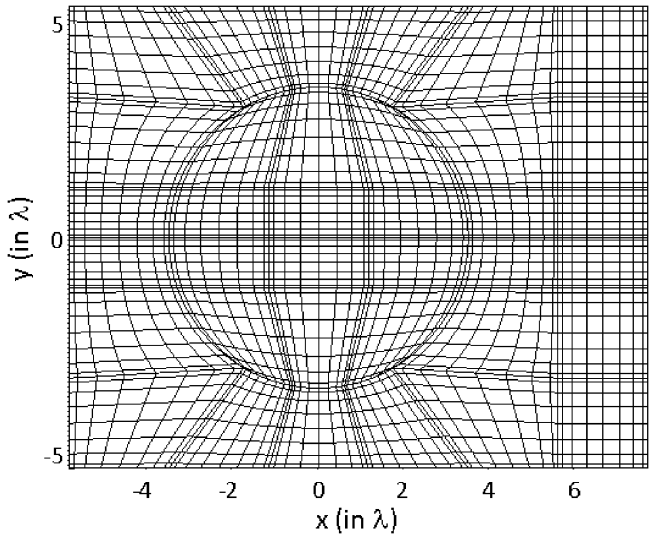

Fig. 3. A possible discretization of the computational domain at $R = 1.5\lambda$, and $N \times N = 9 \times 9$ for each element (here, only elements corresponding to Ω_{FS} and Ω_C are shown).

the free space: (a) $R = 3.5\lambda$, $n = 1.6$, (b) 3-D view of (a), (c) $R = 5\lambda$, $n = 1.6$, and (d) $R = 6.5\lambda$, $n = 1.4$.

It is worth mentioning that after obtaining the solution by SEM from (11a), which represents the scattered field, the incident plane wave is added to the scattered field in the subdomains Ω_C and Ω_{FS} only. This is because of the fact that with the application of SEM in the frequency domain, it is easy to decompose the total field in terms of incident and scattered field components. One can produce the same spatial light distribution under the case where FDTD method is used. We have performed FDTD study and verified the photonic nanojet creations as demonstrated later in this section.

The results presented in Fig. 4 demonstrate the capability of SEM in the analysis of photonic nanojet generation. The input source interacts with the cylindrical object and gets focused at different locations as we change the radius or refractive index of the dielectric material. The focal point appears close to the surface in Fig. 4(a), and it moves away from the back side along the optical axis (y = 0 line) in Fig. 4(c) and (d).

In the next example, we try to emphasize the importance of SEM analysis. For example, when we change the refractive index of the cylinder and keeping the radius constant at 3. 50λ, a resonance mode appears. The spatial field distribution picture is given in Fig. 5.

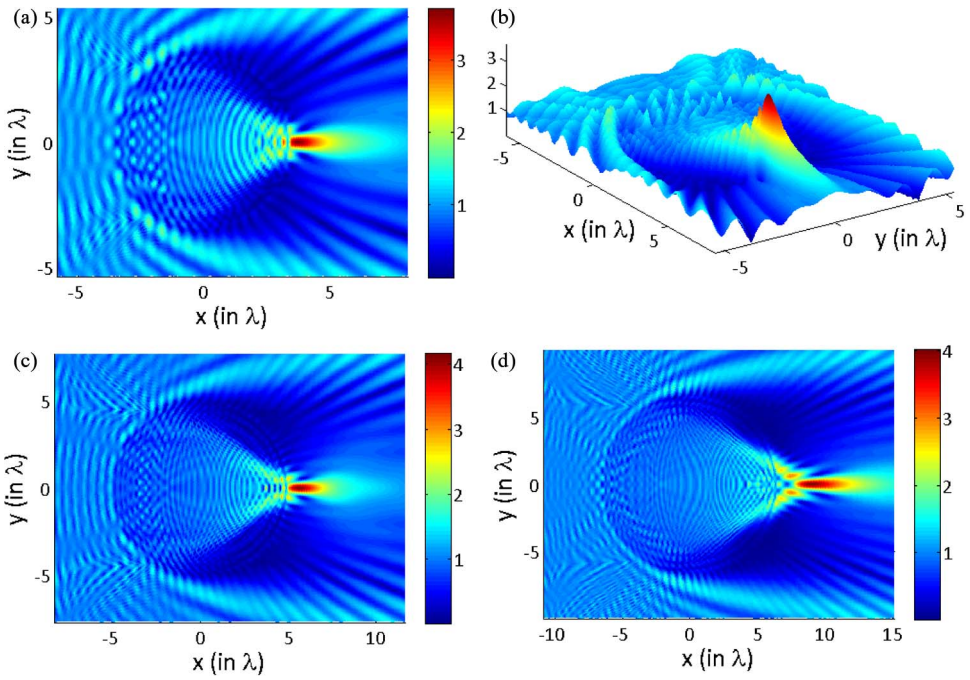

Fig. 4. Visualization of the evolution (spatial distributions) of a photonic nanojet for the following combinations of cylinder radius R of uniform refractive index n embedded within free space. (a) $R = 3.5\lambda$, $n = 1.6$. (b) 3-D view of (a). (c) $R = 5\lambda$, $n = 1.6$. (d) $R = 6.5\lambda$, $n = 1.4$.

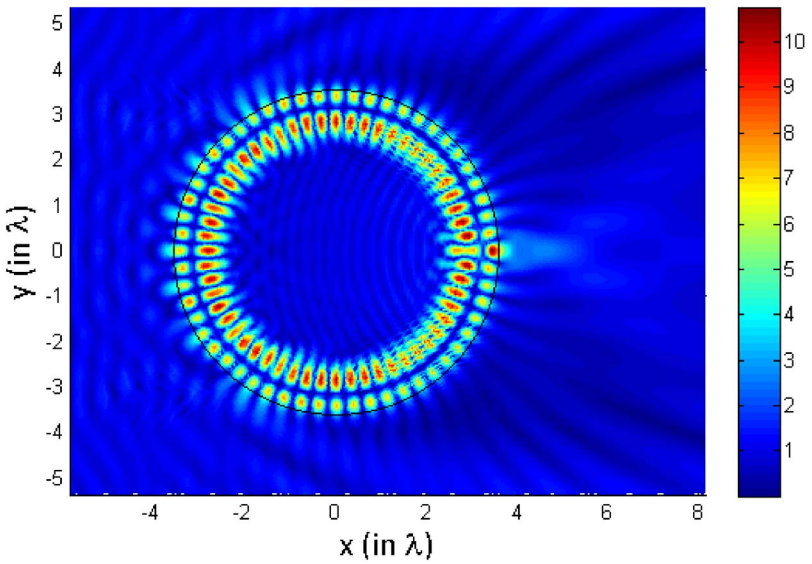

Fig. 5. Visualization of the evolution of a photonic nanojet for $R = 3.50\lambda$ and $n = 1.7$. WGM representation gives $m = 28$ and $l = 2$. Boundary of the dielectric cylinder is shown with a black line.

Fig. 5 shows one of the captured resonance mode supported by a dielectric microcylinder with $R = 3.50\lambda$ and $n = 1.70$. The light focusing action with weak amplitude can be seen at the interior part of the cylinder. On the other hand, strong field localization at around the small cylinder appears with a highly symmetric light distribution in terms of two rings. Similarly, when we change the radius of the cylinder to $R = 4.50\lambda$ then the resonance mode again occurs if the refractive index value becomes 2.0. The result is presented in Fig. 6. Light distribution with five

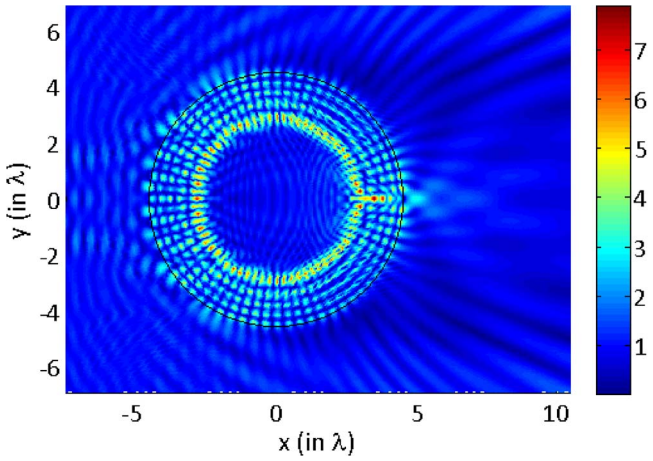

Fig. 6. Visualization of the evolution of a photonic nanojet for $R = 4.50\lambda$ and $n = 2$. WGM parameters are $m = 34$ and $l = 5$. Boundary of the dielectric cylinder is shown with a black line.

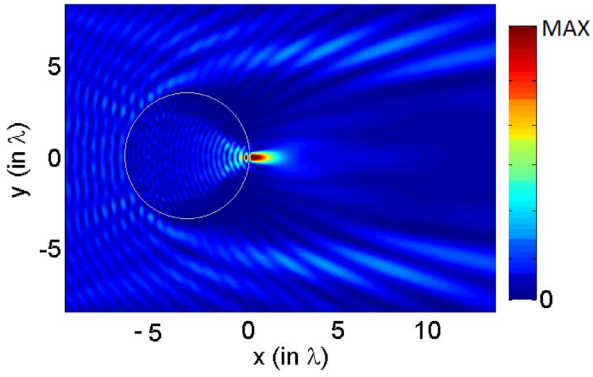

Fig. 7. Visualization of the evolution of a photonic nanojet using 2-D FDTD method for parameters: $R = 3.50\lambda$ and $n = 1.7$. Boundary of the cylinder is shown with a white line.

rings is highly symmetric and strong field localization takes place at the exterior part of the microcylinder. The evanescent field that leaks out of the dielectric cylinder radially is apparent in the plot.

Special cases corresponding to specific radius and refractive index values in Figs. 5 and 6 can be attributed to whispering gallery mode (WGM). The representation WGMm, l indicates a WGM with the azimuthal mode number m and the radial mode number l. The resonance mode with different mode number is confined at the circumference of the cylinder by means of the total internal reflection mechanism. Using that notation we can express Figs. 5 and 6 in terms of WGM resonances. By means of SEM we captured resonance modes as well as photonic nano jets cases. However, we should point out that FDTD method gives us regular light focusing behavior and there is no indication of the creation of resonance mode with the FDTD analysis as it can be observed from Fig. 7.

Plane wave illumination of dielectric microcylinders with FDTD method [26] always produces an expected lensing/focusing effect so that the planar wave front of light gets tilted and focused at the optical axis. Then diffraction of light takes place. Fig. 7 is obtained by implementing two-dimensional FDTD method with the same parameters $R = 3.50\lambda$ and $n = 1.70$. When we compare Fig. 7 with Fig. 5 we realize that the two methods yield different results. While SEM provides WGM behavior as shown in Fig. 5, FDTD data shows photonic nanojet action as demonstrated in Fig. 7.

TABLE 2

Relative errors of SEM and FDM for the problem defined in (30)

FDM		SEM	
N	*Err*	**N**	*Err*
10	0.1840	7	0.0103
20	0.0524	8	0.0012
30	0.0238	9	1.4550E-04
40	0.0135	10	1.6087E-05
50	0.0087	11	2.0749E-06
60	0.0060	12	2.3081E-07
70	0.0044	13	2.5700E-08
80	0.0034	14	2.6247E-09
90	0.0027	15	2.6137E-10
100	0.0022	16	2.4206E-11
110	0.0020	17	2.3182E-12

We should note that while providing FDTD data, the same excitation scheme (i.e., a plane wave excitation) is used for both methods. Different resolutions have been investigated and FDTD method always gives a photonic nanojet but not WGM at around the resonance mode captured by SEM. Why FDTD method cannot capture WGM is because it is a low-order accuracy method and any error will lead FDM (either in the time-domain or frequency-domain) to miss WGM modes. That aspect of FDTD method was investigated in [27]. The detection of WGM resonances with high-Q factors fails with standard FDTD method [27]. As a result, capturing WGM with FDTD becomes intricate.

Capturing these special cases addresses the high accuracy achieved by SEM. On the other hand, the low-order finite difference method couldn't simulate these cases. Obviously, the reason lies in the degree of accuracy of the used numerical method. To emphasize on this point, a comparison is carried out between SEM and finite difference method (FDM). For this purpose, the following 1-D boundary-value problem is considered:

$$\frac{d^2u}{dx^2} + k^2u = 0, \quad x \in [0, 1.1], \text{ with } u(0) = 1,\ u(1.1) = \mathrm{e}^{-jk1.1} \tag{30}$$

where $k = 2\pi/\lambda$, and $\lambda = 1$. The exact solution of this problem is e^{-jkx}. In Table 2, the relative errors for both FDM and SEM are presented as the number of nodes increases in both methods. Obviously, it can be observed that the errors of FDM are slowly decaying although the number of nodes is chosen in the order of 10. On the other hand, SEM shows high accuracy with much less number of nodes. That is, the accuracy obtained by FDM at 100 nodes can be achieved at 8 nodes with SEM. Moreover, from the numerical point of view, as the number of nodes in FDM increases, the condition number of the resulting matrix increases as well. This, in turn, causes the error to decrease at much lower rate even if a very large number of nodes is chosen.

The present manuscript provides formulation of SEM along with PML boundary for a 2-D electromagnetic problem including dielectric scatterer. Observation of photonic nanojets and WGM in dielectric cylinders with SEM is reported for the first time. Comparison of the formulation with FDTD method is given to highlight the advantageous of availability of alternative computational method in photonics. Optical resonators are usually studied by time-domain methods due to advantage of gathering information for a wide frequency range with a single run. On the other hand, due to stair-case problem associated with the Cartesian gridding, numerical errors may include either missing or shifting of the resonant frequencies [27].

The main subject of the paper is to promote the known SEM to the photonic nanojet problem and to demonstrate its high efficiency and accuracy for obtaining WGMs in optical resonator.

Therefore, as an initial step we decided to explore 2-D problem with SEM. The high accuracy offered by the SEM enables us to capture WGMs. The same method can be applied to different cases including but not limited to 3-D structures such as microspheres or micro-ellipsoids. Besides, the presented 2-D analysis can be extended to 3-D if one considers that micro-cylinders have limited height in the third dimension. Finally, 3-D modeling of electromagnetic problems with SEM for different cases are considered in [1] and [2].

6. Conclusion

In this paper, spectral element method is introduced to solve scattering and focusing of light by dielectric microcylinders in two-dimensional frequency domain as well as observing resonance modes. Gauss-Lobatto-Legendre grid is used to construct the basis function. The formulation of perfectly matched layer is also provided together with SEM formulation. In addition, SEM accuracy is demonstrated by solving the scattered field from perfectly conducting cylinders. Within the formulation of SEM, we accurately present and describe field analysis of photonic nanojets in dielectric lossless microcylinders. Strong light focusing at the shadow side of the microcylinder is reported. Advantageous features of SEM allow both observing commonly reported nanojet scenarios and least pointed out transition region where resonance mode appears under certain conditions. The creation of whispering gallery mode types is straightforwardly observed. One may become unaware of these special modes when FDTD method is utilized to numerically solve the scattered field by dielectric microcylinders.

References

[1] J. Lee, T. Xiao, and Q. H. Liu, "A 3-D spectral-element method using mixed-order curl conforming vector basis functions for electromagnetic fields," *IEEE Trans. Microw. Theory Tech.*, vol. 54, no. 1, pp. 437–444, Jan. 2006.

[2] J. Lee and Q. H. Liu, "A 3-D spectral-element time-domain method for electromagnetic simulation," *IEEE Trans. Microw. Theory Tech.*, vol. 55, no. 5, pp. 983–991, May 2007.

[3] S. J. Hesthaven, S. Gottlieb, and D. Gottlieb, *Spectral Methods for Time-Dependent Problems*. Cambridge, U.K.: Cambridge Univ. Press, 2007.

[4] M. Born and E. Wolf, *Principles of Optics*, 7th ed. Cambridge, U.K.: Cambridge Univ. Press, 2002.

[5] L. Novotny and B. Hecht, *Principles of Nano-Optics*. Cambridge, U.K.: Cambridge Univ. Press, 2006.

[6] Z. Chen, A. Taflove, and V. Backman, "Photonic nanojet enhancement of backscattering of light by nanoparticles: A potential novel visible-light ultramicroscopy technique," *Opt. Exp.*, vol. 12, no. 7, pp. 1214–1220, Apr. 2004.

[7] S. Lecler, Y. Takakura, and P. Meyrueis, "Properties of a three-dimensional photonic jet," *Opt. Lett.*, vol. 30, no. 19, pp. 2641–2643, Oct. 2005.

[8] A. Devilez, B. Stout, N. Bonod, and E. Popov, "Spectral analysis of three-dimensional photonic jets," *Opt. Exp.*, vol. 16, no. 18, pp. 14 200–14 212, Sep. 2008.

[9] P. Ferrand *et al.*, "Direct imaging of photonic nanojets," *Opt. Exp.*, vol. 16, no. 10, pp. 6930–6940, May 2008.

[10] M.-S. Kim, T. Scharf, S. Mühlig, C. Rockstuhl, and H. P. Herzig, "Engineering photonic nanojets," *Opt. Exp.*, vol. 19, no. 11, pp. 10 206–10 220, May 2011.

[11] Z. Wang *et al.*, "Optical virtual imaging at 50 nm lateral resolution with a white-light nanoscope," *Nat. Commun.*, vol. 2, no. 3, p. 218, Mar. 2011.

[12] V. R. Dantham, P. B. Bisht, and C. K. R. Namboodiri, "Enhancement of Raman scattering by two orders of magnitude using photonic nanojet of a microsphere," *J. Appl. Phys.*, vol. 109, no. 10, p. 103103, May 2011.

[13] S.-C. Kong, A. Sahakian, A. Taflove, and V. Backman, "Photonic nanojet-enabled optical data storage," *Opt. Exp.*, vol. 16, no. 18, pp. 13 713–13 719, Sep. 2008.

[14] A. M. Kapitonov and V. N. Astratov, "Observation of nanojet-induced modes with small propagation losses in chains of coupled spherical cavities," *Opt. Lett.*, vol. 32, no. 4, pp. 409–411, Feb. 2007.

[15] A. Heifetz, S.-C. Kong, A. V. Sahakian, A. Taflove, and V. Backman, "Photonic nanojets," *J. Comput. Theor. Nanosci.*, vol. 6, no. 9, pp. 1979–1992, Sep. 2009.

[16] A. Taflove and S. Hagness, *Computational Electrodynamics: The Finite-Difference Time-Domain Method*, 3rd ed. Norwood, MA, USA: Artech House, 2005.

[17] G. Kattawar, C. Li, P.-W. Zhai, and P. Yang, "Electric and magnetic energy density distributions inside and outside dielectric particles illuminated by a plane electromagnetic wave," *Opt. Exp.*, vol. 13, no. 12, pp. 4554–4559, Jun. 2005.

[18] A. V. Itagi and W. A. Challener, "Optics of photonic nanojets," *J. Opt. Soc. Amer. A, Opt. Image Sci.*, vol. 22, no. 12, pp. 2847–2858, Dec. 2005.

[19] J. P. Berenger, "A perfectly matched layer for the absorption of electromagnetic waves," *J. Comput. Phys.*, vol. 114, no. 2, pp. 185–200, Oct. 1994.

[20] M. Kuzuoglu and R. Mittra, "A systematic study of perfectly matched absorbers," in *Frontiers in Electromagnetics*. Piscataway, NJ, USA: IEEE Press, 2000.

[21] O. Deville, F. P. Fischer, and E. Mund, *High-Order Methods for Incompressible Fluid Flow*. Cambridge, U.K.: Cambridge Univ. Press, 2002.
[22] J. W. Gordon and A. C. Hall, "Transfinite element methods: Blending-function interpolation over arbitrary curved element domains," *Numer. Math*, vol. 21, no. 2, pp. 109–129, 1973.
[23] C. Schwab, *p- and hp- Finite Element Methods: Theory and Applications in Solid and Fluid Mechanics*. Oxford, U.K.: Oxford Univ. Press, 1998.
[24] I. Babuska and B. Q. Guo, "The h, p, and h-p version of the finite element method: Basis theory and applications," *Adv. Eng. Softw.*, vol. 15, no. 3/4, pp. 159–174, 1992.
[25] G. Karniadakis and S. J. Sherwin, *Spectral/hp Element Methods for CFD*. Oxford, U.K.: Oxford Univ. Press, 1999.
[26] A. F. Oskooi *et al.*, "MEEP: A flexible free-software package for electromagnetic simulations by the FDTD method," *Comput. Phys. Commun.*, vol. 181, no. 3, pp. 687–702, Mar. 2010.
[27] A. V. Boriskin, S. V. Boriskina, A. Rolland, R. Sauleau, and A. I. Nosich, "Test of the FDTD accuracy in the analysis of the scattering resonances associated with high-Q whispering-gallery modes of a circular cylinder," *J. Opt. Soc. Amer. A, Opt. Image Sci.*, vol. 25, no. 5, pp. 1169–1173, May 2008.